Research Article | Vol. 27, No. 5 | 4 Mar 2019 | OPTICS EXPRESS 6184
Optics EXPRESS

Telecentric broadband objective lenses for optical coherence tomography (OCT) in the context of low uncertainty metrology of freeform optical components: from design to testing for wavefront and telecentricity

DI XU,* ROMITA CHAUDHURI, AND JANNICK P. ROLLAND

[1]The Institute of Optics, University of Rochester, Rochester, NY 14620, USA
*dxu7@ur.rochester.edu

Abstract: Freeform optical components enable significant advances for optical systems. A major challenge for freeform optics is the current lack of metrology methods with measurement uncertainty on the order of tens of nanometers or less. Towards addressing this challenge, optical coherence tomography (OCT) is a viable technique. In the context of low uncertainty metrology, the design requirements pertaining to the sample arm of an OCT metrology system are explicitly addressed in this paper. Two telecentric, broadband, diffraction limited, custom objective lens designs are presented with their design strategies. One objective lens was fabricated and experimentally tested for wavefront performance and telecentricity. This lens demonstrates near diffraction limited performance and a maximum deviation from telecentricity of 8.7 arcseconds across the full field of view, correlating to measurement uncertainty of less than 12 nm in simulation. The telecentricity test method developed completes the loop with respect to the design requirements and strategies presented and provides further intuition for telecentric lens designs in general.

1. Introduction

Freeform optical components are gaining traction as they enable advances for optical systems in both performance and packaging [1–4]. A major challenge for freeform components is the need for non-contact figure metrology that has sufficiently low measurement uncertainty, is flexible across different surface shapes, and can accommodate for large sag and slope variations. As a rule of thumb, the measurement uncertainty of the metrology instrument should ideally be an order of magnitude lower than the specified tolerance on the optic. As typical figure tolerances may be on the order of λ/2 to λ/4 [5], where λ is the wavelength of operation, the uncertainty of the figure metrology should be at most on the order of tens of nanometers for the visible spectrum. Furthermore, it is also desired that the metrology has high dynamic range in terms of surface roughness to not only measure finished components but also to provide iterative feedback during the manufacturing process.

Towards addressing this challenge, we have been investigating custom Fourier domain optical coherence tomography (OCT) systems for the metrology of freeform optical components [6,7]. In this technique, the low coherence characteristics of broadband light sources enable optical sectioning through depth. With a sufficiently broad spectral bandwidth and advanced post-processing algorithms, the localization of axial measurements may be pushed to the single digit nanometer level [8]. In the context of metrology for freeform optical components, the axial measurements correspond directly to the measured freeform sag after accounting for the reference surface. Lateral scanning of the beam across the sample enables three-dimensional volumetric measurements, resulting in point cloud measurements of the freeform under test. By applying telecentric scanning that is the focus of this paper, the OCT

#352469 https://doi.org/10.1364/OE.27.006184
Journal © 2019 Received 19 Dec 2018; revised 1 Feb 2019; accepted 2 Feb 2019; published 20 Feb 2019

Optics EXPRESS

metrology system does not require a priori knowledge of the surface under test, thus enabling flexibility across different surface shapes with little to no additional modifications. The range of measurable sag may be up to millimeters and the range of measurable slope may be up to tens of degrees, making this technique especially suitable for small optical components that are one to two inches in diameter. Moreover, OCT is sensitive to both specular and diffuse light signals [9], enabling measurements of both rough and smooth optical surfaces along the manufacturing process chain from grinding to polishing.

To realize an OCT metrology system with the desired characteristics, multiple unique design requirements must be investigated and quantified. System design aspects are seldom discussed in typical OCT literature where the focus is on the application and experimental results [10–12]. However, hardware instrumentation design and optimization play a critical role in determining the measurement quality and warrant careful investigation. In this work, the specific design requirements placed on the sample arm of an OCT metrology system and their impact on the measurement uncertainty are explicitly addressed specifically for the case of pre-objective telecentric scanning, where an objective lens focuses the input collimated beam into the sample volume and rotary mirror device(s) enables beam steering via angular control at the objective lens' pupil plane or its optical conjugates. The impact of telecentricity, distortion mapping, image plane flatness, and residual wavefront error on the measurement uncertainty is analyzed.

Aside from the imaging requirements, signal throughput is another critical design consideration as it directly determines the range of measurable slopes and surface roughness. A typical OCT sample arm configuration is monostatic, i.e. the numerical aperture (NA) of the probing beam forms the solid angle cone that collects the back-reflected or back-scattered light signal. In other words, the typical OCT sample arm acts as both illumination and imaging systems. A challenge in signal collection arises when using OCT to measure optical surfaces when the optics has high slopes as well as when the optical surfaces are polished to be highly specular. One intuitive method to overcome this challenge is to increase the NA. However, increasing the NA typically reduces the depth of focus and consequently the range of measurable sag. Another commonly utilized method is to rotate the objective lens such that the probing beam remains normal to the sample surface [13,14]. This rotatory degree of freedom is an additional source of uncertainty and in addition it makes it necessary to have a priori knowledge to trace the surface. A bistatic configuration may be envisioned where the illumination and imaging systems are separate and independent of one another. However, this configuration is challenging for interferometry because unavoidable as-built differences result in optical path differences (OPD) that add to measurement error, as will be discussed in Section 2.2. We developed and report here a unique pseudo-bistatic scanning configuration that does not require rotation of the objective lens and retains the necessary depth of focus while maximizing signal throughput, enabling the measurement of arbitrarily smooth optical surfaces over a range of local slopes.

With respect to the necessary specification requirements for low uncertainty freeform metrology laid out in this work, it was found that commercially available objective lenses do not satisfy these requirements especially in terms of high telecentricity across scan and wide spectral bandwidth over which diffraction limited performance is achieved. Existing off-the-shelf OCT objective lenses rarely quantify telecentricity and assume that the user will compensate for it by adjusting the positioning of the rotary mirror device. This assumption is flawed, as will be addressed in detail in Section 2. Highly telecentric lenses exist for the field of machine vision; however, they are typically bi-telecentric and are therefore unsuitable for pre-objective scanning. In this work, two objective lens designs were developed; one was optimized for a large scanning field of view (FOV), while the other was optimized for a large NA and investigates the extent to which the pseudo-bistatic configuration may be applied in practice while balancing manufacturing sensitivity and cost. The design strategy for achieving the necessary requirements is presented and discussed.

Optics EXPRESS

In addition to the design aspects, the large FOV objective lens was toleranced, fabricated, and experimentally validated for both wavefront error and telecentricity. The telecentricity measurement method presented here is a single-shot interferometric method. Currently, the most prevalent method for measuring telecentricity is by using the lens under test to image a resolution target at different axial distances. This conventional method is mostly limited to testing bi-telecentric lenses and is limited in angular resolution and measurement uncertainty, which are determined by the detector pixel size, the travel range of the resolution target, and the quality of this linear travel. The telecentricity measurement method developed here requires no moving elements and is capable of testing lenses that are telecentric in either object or image space as well as bi-telecentric lenses. In addition, the method presented here is capable of not only quantifying telecentricity but also revealing any mis-alignment errors within the lens assembly. The telecentricity experimental results complete the loop with respect to the design strategy described and provide further intuition for telecentric lens designs in general.

2. Impact of telecentricity, distortion mapping, residual wavefront error, and image plane flatness on measurement uncertainty

For this study in the context of figure metrology, uncertainty is quantified in simulation modelling as the deviation of the as-measured surface from the known nominal prescription. In experiment, this uncertainty includes both accuracy and precision of the measured value with respect to the unknown ground truth. Throughout this work, the image space in optical design terminology refers to the sample space with the freeform under test. It is emphasized that the four aspects analyzed in this section have no direct causality correlation, as will be addressed in detail.

2.1. Impact of telecentricity and distortion mapping

The telecentricity characteristics and distortion mapping of the objective lens directly determine the resulting beam location mapping across lateral scans, which need to be constrained in design and accounted for in the measurement of the sample optic. Telecentricity is quantified as the absolute value of the maximum chief ray angle at the image plane across the lateral scanning FOV. Distortion mapping is evaluated as the deviation from an ideal f-θ mapping of the actual beam position on the image plane or another evaluation plane through focus. The f-θ mapping that creates a linear mapping of the scan angle to the beam position is typically desired with scan lenses.

In experiment, we control the rotary mirror device to perform lateral scanning and obtain volumetric measurement data. The data matrix is therefore organized by the location of the beam as calculated using the mirror angle. Having non-zero distortion translates to having uncertainties in this location mapping in the form of the measurement being “squeezed” or “stretched” artificially, resulting in measurement artifacts not actually present on the surface under test. Even more problematic is when non-zero distortion is combined with non-telecentricity, in which case the distortion mapping varies through focus and results in different mapping errors at different axial planes. Moreover, unless the lens is telecentric, having zero distortion at the best focus image plane does not result in zero distortion through focus. The impact of telecentricity and distortion on the location of the beam on the sample is illustrated schematically in Fig. 1.

In optical design, it is likely under-appreciated that it is generally difficult to have both zero distortion and strict telecentricity at the same time, especially for designs with significant FOVs. As illustrated in Fig. 1, between the zero distortion with non-telecentricity case (red) and the non-zero distortion with strict telecentricity case (blue), experimental calibration is more straightforward when strict telecentricity is achieved since the beam centroid location displaces by a constant amount through focus. This aspect determines that for the objective

Optics EXPRESS

lens design it is best to prioritize telecentricity and evaluate distortion towards the end of the optimization process.

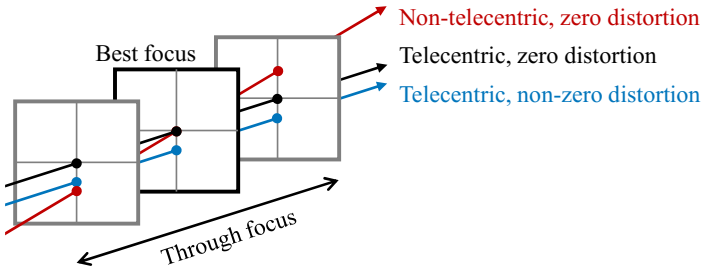

Fig. 1. Schematic showing beam centroid location variations through focus at a single point in a lateral scan for possible telecentricity and distortion characteristics of an objective lens.

Within this design criteria, we next quantify the tolerance on non-telecentricity with respect to the measurement uncertainty. As OCT with telecentric scanning is a point cloud technique that is largely decoupled from the surface under test, it does not matter to the instrument whether the sample surface has rotational invariance. To this end, a simple model with a parabolic surface is shown as follows. A parabola is chosen here to yield an analytic solution, while the results remain meaningful for other surface shapes of similar sag and slope values. For this model, the best focus plane is placed halfway of the total surface sag with zero-distortion at this plane. The chief ray angles of incidence θ are assumed to be zero on-axis and linearly increasing toward the edge of the scanning FOV, a scenario not uncommon for a scan lens design.

Figure 2(a) shows half of a one-dimensional slice through the parabolic sample. It can be seen from the shaded triangle in Fig. 2(a) that

$$\tan(\theta) = \frac{y' - y}{z_{\max}/2 - sag(y')} \tag{1}$$

$$sag(y') = y'^2/(2R) \tag{2}$$

where y is the beam location if strictly telecentric, y' is the actual beam location accounting for deviation from telecentricity, and $z_{\max}$ is the maximum surface sag. The functional dependence of y' on θ may be solved using Eq. (1) and Eq. (2) to yield

$$y'(\theta) = \frac{-1 + \left\{1 + 2\cdot[y + (z_{\max}/2)\tan(\theta)]\cdot\tan(\theta)/R\right\}^{1/2}}{\tan(\theta)/R} \tag{3}$$

The measurement error is evaluated as

$$\Delta = sag(y') - sag(y) \tag{4}$$

The specifications for the parabola are chosen such that the corresponding maximum sag and slope are representative of the values for freeform optical components that we have surveyed [3,15–17]. For a Φ30 mm parabola with 2 mm maximum sag and 15° maximum slope (i.e. R = 56.25 mm), the measurement errors with a maximum non-telecentricity of 0.02° are shown in Figs. 2(b) and 2(c). As expected, the maximum error appears at the location of highest slope and largest non-telecentricity. For these specific simulation parameters, the errors are well contained within ± 30 nm up to approximately 25 mm in diameter, as shown by the green dotted lines in Fig. 2(c).

Optics EXPRESS

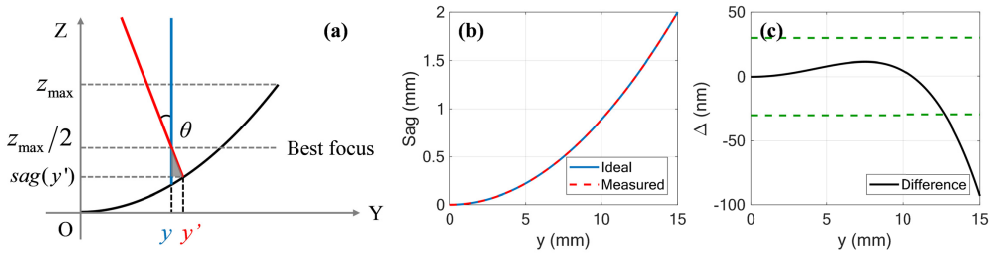

Fig. 2. (a) Part of a 1D slice through a parabolic sample surface, showing the effects of non-telecentricity on beam-location mapping (exaggerated). For a parabola with R = 56.25 mm and a maximum non-telecentricity of 0.02°, the measured surface is plotted against the ideal in (b) with the measurement errors shown in (c), where the green dotted lines bound ± 30 nm.

2.2. Impact of residual wavefront error and image plane flatness

As OCT is an interferometric technique, the sag of the sample under test at a specific location in the lateral scan is encoded as the OPD between the sample arm and the reference arm. Therefore, any factor other than the sample that may alter the optical path length of one arm while not the other will introduce uncertainty into the sag measurement. Of consideration are the aberrations introduced by the optical components in the path of the light beams. These aberrations will not only affect the optical path length traversed by the beam but also affect the focus of the beam on the sample, i.e. the lateral resolution. The objective lens should therefore be designed to have diffraction limited performance as-built, defined here as having RMS wavefront error (RMSWE) of less than 0.07λ, where λ is the wavelength of operation.

Another consideration is the mismatch between the reference and sample arm, since in practice no two optics are exactly alike. A method to mitigate for this aspect is to fold the two arms into one, i.e. by having a common-path configuration, where the reference surface is as close to the sample surface as possible optically within the depth of focus of the probing beam. This aspect translates to the requirement of having a long working distance, as will be shown in Section 4, to accommodate for a beam-splitting element after the objective lens. A corollary advantage of this configuration is that it is now possible to have a non-flat reference surface, enabling the use of reference spheres or conics, base toroids, or even freeform masters.

The third consideration is the optical path length of the beam as it is scanned across the FOV. In this context with a typical collimated laser beam input, the image plane refers to the best fit surface for the across-scan focal spots conjugate to infinity. In other words, the real image plane is the surface formed by the focal spots across the lateral scanning FOV that marks equal optical path lengths to the entrance pupil. As the measurand is the difference between the optical path lengths of the reference and sample arms, it becomes apparent that the image plane is in fact the zero OPD surface between the reference and the sample. This surface is more likely to be curved rather than planar due to the presence of field curvature that is inherent in almost all imaging optical designs unless specifically accounted for via balancing of optical power between elements and/or balancing with other aberrations. The latter is referred to as flat field solutions. It is worth noting that field curvature reduces to Petzval curvature in the absence of astigmatism.

To further illustrate this point, a simple setup optimized for telecentric scanning with an off-the-shelf achromatic doublet (AC508-100-B, Thorlabs Inc., NJ, USA) is shown in Fig. 3. With incoming light direction from left to right, one may place a rotary mirror scanner at the accessible entrance pupil to use this doublet as an objective lens in telecentric scanning mode. Regardless of the evaluation surface I' which the optical designer can choose quasi-arbitrarily, the real image plane for an OCT system is the surface I from which the OPD is measured, resulting in measurement artifacts if this curvature is not accounted for. A flat sample measured with this objective lens will appear to be curved in the obtained data. To give an

Optics EXPRESS

order of magnitude of this error, at surface *I′* and with an operation wavelength of 900 nm, the optical path length of the central ray of the on-axis ray bundle is 208.281 mm while that of the full field off-axis ray bundle is 208.338 mm, resulting in a measurement error artifact of 57 μm at the edge of the field which is approximately three orders of magnitude worse than the required measurement uncertainty as laid out in Section 1.

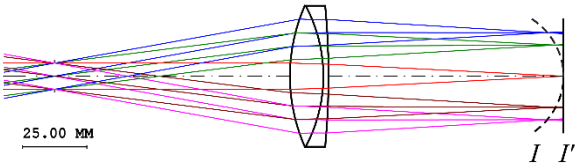

Fig. 3. Illustration of field curvature for a sample arm setup optimized for high telecentricity with an off-the-shelf achromatic doublet. Surface *I* indicates schematically the surface at which the central rays from each ray bundle across scans achieve equal optical path lengths (not to scale). Surface *I′* is an arbitrarily selected performance evaluation surface.

It is worth noting that the setup of Fig. 3 was optimized for high telecentricity, demonstrating that the measurement error artifact shown is strictly due to a non-flat image plane rather than non-telecentricity with no causality correlation between the two. This means that while one may compensate for telecentricity in practice by adjusting the axial position of the rotary mirror device, it is not consequent that diffraction limited performance will be maintained across a flat image plane. Therefore, in the optical design process for an OCT objective lens, one must optimize for diffraction limited performance across a planar evaluation surface as well as high telecentricity simultaneously.

3. Pseudo-bistatic scanning configuration for enhanced signal collection

As outlined in Section 1, signal throughput is another critical design consideration especially for finished optical surfaces of high slope that may have RMS surface roughness on the order of single digit nanometers or less. A unique pseudo-bistatic scanning configuration was developed to enable measurement of arbitrarily smooth optical samples without rotating the objective lens nor the sample, while maintaining the necessary depth of focus.

In this pseudo-bistatic scanning configuration, the objective lens is used with a probing light beam of the same NA as one may use for a typical monostatic configuration, denoted as NA_p. This NA_p may be determined based on the required depth of focus or diffraction limited spot size. However, the objective lens is to be designed such that it is diffraction limited over a larger collection NA that is responsible for collecting the back-reflected light signal. A schematic layout of this configuration is shown in Fig. 4.

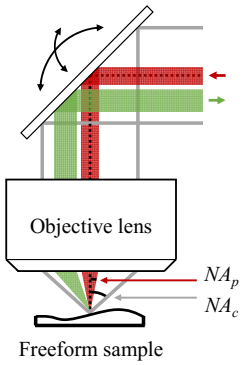

Fig. 4. Schematic of the pseudo-bistatic scanning configuration showing the incoming probing beam (red) and the collected specular reflection (green), both within the collection aperture NA_c for which the objective lens was designed.

Optics EXPRESS

The collection NA, denoted as NA_c, is given by

$$NA_c = \sin(\theta_p + 2\alpha_{\max}), \tag{5}$$

where θ_p is the angle corresponding to NA_p and $\alpha_{\max}$ is the maximum slope angle one expects the sample surface to have. A corollary design criterion is that the system using this objective lens should also be designed accounting for NA_c. In practice, this system level requirement is more readily achieved in optical fiber-based systems compared to free-space ones.

As can be seen, though the optical components making up the illumination and imaging systems are the same, the sub-sections of those components experienced by the illumination and imaging beams are different, though this difference is constrained by the requirement of diffraction limited performance over NA_c. As such, this configuration is referred to as pseudo-bistatic.

Under this configuration, the specularly reflected light is captured by the objective lens up to the slope angle $\alpha_{\max}$ while maintaining the required depth of focus. As a result, this configuration enables the measurement of arbitrarily smooth samples within its design specifications. By having the objective lens well-corrected over the NA_c, it is ensured that the OPD introduced from the optical lens system itself is minimized. A corollary advantage of this configuration is that it removes the need to rotate the objective lens to follow the local normal of the sample surface up to the slope angle $\alpha_{\max}$, thus eliminating errors that may result from the rotary actuation as well as the need of *a priori* knowledge of the surface. Moreover, as this configuration uses the same probing beam as that for a typical monostatic configuration, it also enables the integration of lenses designed for either configuration under one instrument to extend the measurement dynamic range in terms of sample slope and surface roughness.

4. Telecentric and broadband achromatic objective lens designs

Aside from the specification targets laid out in Section 2, a broad bandwidth of 360 nm centered at 900 nm was also required for our application to achieve 1 μm axial coherence length with a Gaussian laser source profile. A 2 mm depth of focus in air was also required in accordance with sag ranges found on existing freeform optics, translating to an image space probing beam NA_p of 0.0324. Under these specification requirements, we report here two custom objective lens designs that are both highly telecentric and broadband diffraction limited over a flat image plane. One design is for a large FOV monostatic configuration, while the other is for the pseudo-bistatic configuration described in Section 3 with a large NA_c.

With respect to the design strategy for both lenses, it is emphasized that telecentricity is constrained from the beginning of the optimization process. This may be implemented by applying specific constraints to the optimizer merit function and/or by choosing a starting point design that was optimized with some telecentricity target. The specific constraint applied should be one that allows for both positive and negative angular values to enable a stable optimization process. For both design forms, it was found that telecentricity constraints greatly impact the design solutions found and it was in general difficult to recover telecentricity if not designed for without significant trade-off from the other performance specifications.

With the level of telecentricity requirement indicated in Section 2.1 as guideline, the large FOV objective lens design was pushed for even more stringent telecentricity values nominally to investigate its design limits and to allow for manufacturing margin. It was found that by slowly walking the design form, telecentricity may be pushed to be on the order of 1″ (1 arcsecond = 1/3600 degrees) while maintaining diffraction limited performance over a flat image plane that is 40 mm in diameter. The large NA objective lens functions as a design study to investigate the extent to which the pseudo-bistatic configuration may be applied especially in terms of its scanning FOV. To measure a sample with 15° maximum slope, a

Optics EXPRESS

NA_c of 0.55 is required as calculated using Eq. (5). It was found that a significant FOV could not be achieved without evolving the design form into the lithography lens regime and the final FOV was required to be drastically reduced to 88 μm in diameter. This finding indicates that the pseudo-bistatic configuration may be best suited for a coordinate measuring machine framework where lateral mechanical actuation enables scanning over the freeform part. Nevertheless, the elimination of the rotary degree of freedom and the ability to capture the specular reflection signal are expected to contribute to reductions in measurement uncertainty. With the reduction in the scanning FOV, the telecentricity constraint for the large NA objective lens was consequently loosened to up to 0.1°, which corresponds to approximately 2 nm maximum uncertainty when applied to the simulation model shown in Section 2.1.

The achieved specifications for both designs are shown side by side in Table 1 for ease of comparison. The layout of the two designs are shown in Fig. 5 and their detailed prescriptions are given in Tables 2 and 3. The key performance metrics of the two objective lens systems are visualized in Fig. 6. The nominal RMSWE achieved for the large FOV objective lens is 0.0404λ ± 0.0084λ with a maximum of 0.0538λ. The nominal telecentricity achieved is 0.8″ ± 0.4″ with a maximum of 1.3″. The large FOV objective was also designed to have a large 100 mm working distance to allow for a beam-splitting element between the lens and the freeform sample. For the large NA objective lens, the nominal RMSWE achieved is 0.0345λ ± 0.0030λ with a maximum of 0.0406λ. The nominal telecentricity achieved is 0.046° ± 0.016° with a maximum of 0.068°. As both lens systems are rotationally invariant, telecentricity is shown across the lateral scan in one direction in Figs. 6(c) and 6(d) and is representative over the full two-dimensional scanning FOV.

Table 1. Specifications and achieved nominal performance for the two objective lens designs.

Specification parameter	Large FOV objective lens	Large NA objective lens
1. Spectral range (nm)	720 – 1080	720 – 1080
a. Design wavelengths (nm)	720, 900, 1080	720, 900, 1080
b. Reference wavelength λ (nm)	900	900
c. Weighting	1:1:1	1:1:1
2. Entrance pupil diameter (mm)	10	5.5
3. Effective focal length (mm)	154	5
4. Image space NA	0.0324	0.55
5. Full scanning FOV, diameter (mm)	40	0.088
6. Full optical scan angle (°)	± 7.4	± 0.5
7. RMSWE, nominal maximum (λ)	0.05	0.041
8. Telecentricity, nominal maximum (°)	0.00036	0.068
9. Vignetting (%)	0	0
10. F-θ distortion, nominal maximum (μm)	33.13	0.037
11. F-θ distortion, nominal maximum (%)	0.16	0.15
12. Overall length, vertex to vertex (mm)	160	12
13. Working distance (mm)	100	2.5

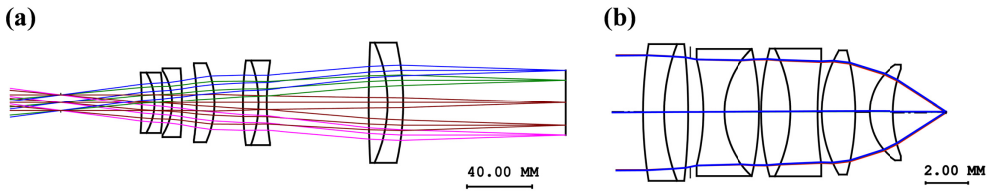

Fig. 5. Layout drawing of (a) the large FOV and (b) the large NA objective lens design.

Optics EXPRESS

Table 2. Prescription for the large FOV objective lens design.

Lens #	Surface #	Radius (mm)	Thickness (mm)	Material	Diameter (mm)
L1	S1	–250.969	7.80	S-LAH58	34.9
	S2	–37.211	5.00	S-TIM22	34.9
	S3	–151.188	5.66	Air	34.9
L2	S4	–37.216	6.00	S-FSL5	39.8
	S5	–263.560	9.02	Air	39.8
L3	S6	–156.358	10.80	S-LAH58	45.9
	S7	–61.143	17.34	Air	45.9
L4	S8	189.929	9.50	S-BSM2	49.2
	S9	–75.701	5.00	S-TIH4	49.2
	S10	155.244	63.22	Air	49.2
L5	S11	763.000	11.50	S-LAM2	70.2
	S12	–89.198	9.50	S-TIH11	70.2
	S13	–170.067	100.00	Air	70.2

Table 3. Prescription for the large NA objective lens design.

Lens #	Surface #	Radius (mm)	Thickness (mm)	Material	Diameter (mm)
L1	S1	20.327	1.00	S-PK57Q1	6.2
	S2	8.939	1.14	S-NLAF2	6.2
	S3	–28.479	0.10	Air	6.2
L2	S4	–10.193	1.00	S-NKZFS4	5.8
	S5	4.152	1.68	CAF2	5.8
	S6	–13.494	0.10	Air	5.8
L3	S7	11.525	1.39	S-NKZFS4	5.8
	S8	–6.622	1.30	S-SF4	5.8
	S9	17.372	0.19	Air	5.8
L4	S10	5.784	1.60	O-SFPL51	5.6
	S11	–11.144	0.69	Air	5.6
L5	S12	2.721	1.13	S-NSK11	4.2
	S13	5.892	2.50	Air	4.2

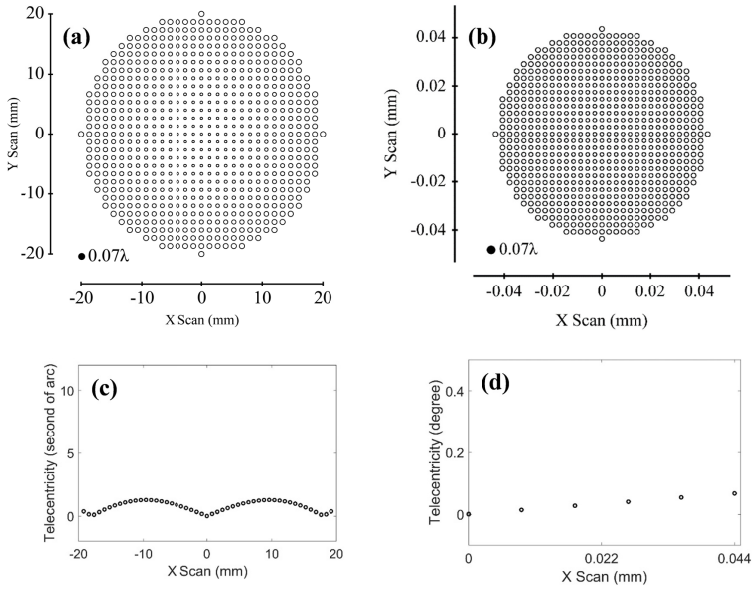

Fig. 6. Full field display of the nominal achieved RMSWE for (a) the large FOV and (b) the large NA objective lens, both showing diffraction limited performance. Achieved nominal telecentricity for (c) the large FOV and (d) the large NA objective lens.

The nominally achieved telecentricity values for both designs were evaluated in relation to the measurement uncertainty using the simulation model of Section 2.1, the results of which

Optics EXPRESS

are shown in Fig. 7. The maximum measurement error on the parabolic part due to the nominal residual non-telecentricity from the large FOV objective lens is 0.4 nm while that with the large NA objective lens is 0.9 nm, affording sufficient margins for manufacturing tolerances with respect to telecentricity.

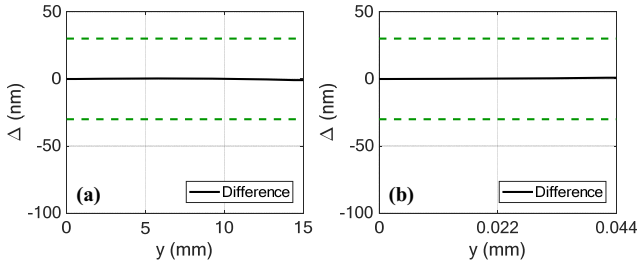

Fig. 7. Simulated measurement uncertainty on the parabolic sample surface of Section 2.1 with the achieved nominal telecentricity of (a) the large FOV and (b) the large NA objective lens across their respective scanning FOVs up to the sample boundary. The green dotted lines bound ± 30 nm for ease of comparison with Fig. 2(c).

5. Fabrication and testing

The large FOV objective lens was selected for fabrication and testing. This choice was driven by several factors. First, the large FOV design enables lateral scanning over a significant sample area by using rotary mirror device(s) at its accessible entrance pupil plane or its optical conjugates. This optical scanning configuration eliminates the need of mechanical actuation of the sample up to its scanning FOV, which consequently eliminates noise sources associated with the mechanical actuation. Scanning via rotary mirror device(s) is also in general faster than mechanical stages. Secondly, the broad spectral bandwidth necessitates a free-space OCT system due to the current lack of commercially available fiber optic components, for example circulators and couplers/splitters, that can accommodate this spectral range. While the large NA objective lens enables the pseudo-bistatic configuration, under the free-space architecture it quickly becomes resource intensive as all other system sub-assemblies need to accommodate for a beam diameter that is approximately 20x bigger than that with the large FOV objective lens in the monostatic configuration. As such, the large NA objective lens is more suited for fiber-based systems while the large FOV objective lens may be used for both fiber-based and free-space systems. The trade-off with the large FOV objective lens is that it may be challenging to measure very smooth optical surfaces with high slope. However, it is worthwhile to investigate first with this objective lens to benchmark measurement uncertainty. As technology advances, an integrated system is envisioned where the two objective lenses may be mounted together under one instrument to extend the measurement dynamic range in terms of sample surface roughness.

5.1. Tolerancing analysis

During the design process, manufacturability was controlled for by monitoring the angles of incidence of the rays on each surface of the design and reducing them where necessary. Tolerance sensitivity was also evaluated and controlled during optimization using built-in functions of the optical design software (e.g. SAB and SN2 for CODE V). Tolerancing analysis was performed for polychromatic RMSWE as well as telecentricity across the full FOV. The image plane de-space and the aperture stop de-space were used as the only compensators. The final tolerance values chosen are generally considered to be in the precision category range of tolerances [5] and are shown in Table 4.

It was found that the image plane de-space compensator was effective for the polychromatic RMSWE tolerancing with no effect on the telecentricity tolerancing and vice versa for the aperture stop de-space compensator. The two tolerancing analysis were therefore

Optics EXPRESS

performed independently of one another under the same set of tolerance values. The cumulative yield results are shown in Fig. 8. Larger than 90% yield is achieved for both diffraction limited RMSWE and telecentricity of 0.02° (72″).

Table 4. Tolerance table for the large FOV objective lens.

Parameter	Value
Centered tolerances	
Glass material (n_d, v_d)	± 0.0005, ± 0.5%
Radius (larger of two)	± 0.1% or 3 fringes (at 546.1 nm)
Irregularity (fringes)	0.5
Center thickness for lens elements (mm)	± 0.050
Center distance for air spaces < 100 mm (mm)	± 0.050
Center distance for air spaces ≥ 100 mm (mm)	± 0.100
Outer diameter (mm)	+ 0.000/-0.025
Clear aperture	90%
Decentered tolerances	
Wedge, total indicated runout (mm)	± 0.010
Tilt (rad)	± 0.001
Element decenter (mm)	± 0.025
Roll, doublet (mm)	± 0.010

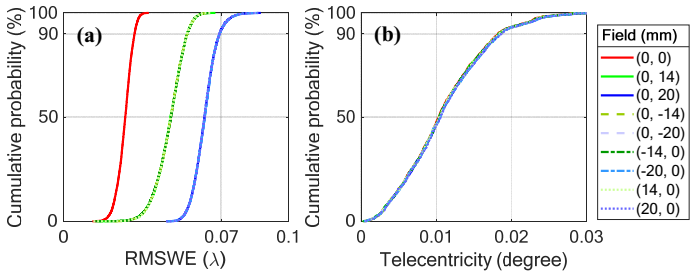

Fig. 8. Tolerancing analysis for the large FOV objective lens under the tolerances given in Table 4 for (a) polychromatic RMS and (b) telecentricity. The field points used are shown in the legend that applies to both plots. Larger than 90% yield is achieved for diffraction limited RMSWE and for 0.02° maximum non-telecentricity.

5.2. Assembly and wavefront testing method and results

The individual lens elements were fabricated and anti-reflection (AR) coated at Kreischer Optics, Ltd. (IL, USA). Since no lens elements were used as compensators, the opto-mechanical mounting is a monolithic barrel that was designed and fabricated at Bauer Associates, Inc. (MA, USA). The barrel was designed with mounting seats to hold the individual lens elements vertically with gravity. Three radial holes were made around the barrel at each lens element location to allow for the injection of ultraviolet (UV) curable epoxy. The assembled lens system underwent wavefront testing prior to epoxy injection and UV curing.

The lens assembly and experimental setup for wavefront testing is shown in Fig. 9(a). An aluminum spacer tube was precision machined to position a laser fiber output at the image plane of the objective lens to within ± 100 µm. The laser (CPS808S, Thorlabs Inc., NJ, USA) outputs at 808 nm, which is within the design wavelength range of the objective lens. The laser is coupled into a multimode fiber, the output tip of which acts as a quasi-point source. The objective lens is pupil matched to within ± 1 mm to a commercial camera (Fujinon HF16SA, Fujifilm, Japan), the output of which is monitored via a computer. The camera lens speed is fixed at F/1.6, which results in a magnification ratio of 9.625 with the objective lens speed of F/15.4. At the laser wavelength of 808 nm, the diffraction limited spot diameter on the camera detector is calculated to be 3.15 µm which is smaller than the detector pixel size of 3.45 µm. This configuration means that if the objective lens was made and assembled to

Optics EXPRESS

achieve diffraction limited performance, then only one single pixel should light up at each field point.

The results of the wavefront testing are shown in Fig. 9(b). As can be seen, light is mostly confined to a single pixel, indicating diffraction limited performance toward the center of the field and near diffraction limited performance toward the edge of the field. At the same time, it can be seen from Fig. 9(c) that the intensity at the full-field is approximately 50% to 60% as that at on-axis. Figure 9(c) plots the ensquared energy within a 9x9 grid centered at the pixel of highest intensity for each field point, normalized to the on-axis intensity. The lens barrel was audited to confirm that it did not vignette across the field. The maximum 2 mm pupil mis-match between the objective lens and the camera lens was found to result in approximately 3% vignetting, which is an order of magnitude smaller than the observed decrease in intensity. It was deduced that the most plausible reason is due to the camera lens used. As the camera lens is one that was designed for the visible spectrum and therefore most likely not AR coated for the near infrared (NIR) regime, one may expect a coating loss of 5% per air/glass interface. The camera lens is estimated to have 4 to 5 lens elements, which results in final transmittance of 66% to 60% respectively, which matches the order of magnitude of the observed intensity change. The wavefront testing results indicate that the objective lens has been manufactured and assembled to specifications. The objective lens assembly was subsequently epoxied and UV cured.

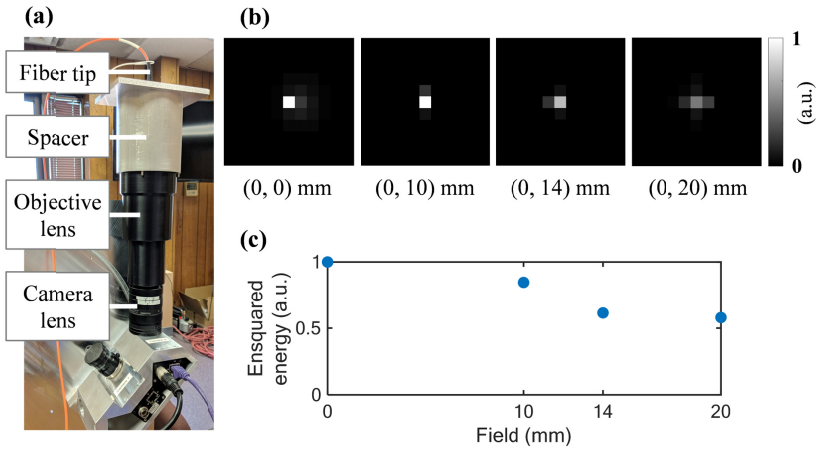

Fig. 9. (a) Wavefront testing setup for the objective lens assembly. (b) Results of the wavefront testing shown in (a) across FOV, showing near diffraction limited performance. (c) Plot showing the decrease in light intensity across the FOV, which was found to be caused by the camera lens used and not by the objective lens' opto-mechanical housing. The results indicate that the objective lens has been manufactured and assembled to specifications.

5.3. Telecentricity testing method and results

The principle of the single-shot test method developed for measuring telecentricity is as follows. The lens drawing of the large FOV objective lens design from Fig. 5(a) is reproduced below in Fig. 10(a). As can be seen, the central ray of each ray bundle across the scanning FOV is quasi-parallel to the optical axis in the image space with light direction from left to right. This suggests that if one were to send in a collimated wavefront from right to left, the lens should be able to form a well-corrected focus at the original pupil plane, as shown in Fig. 10(b). Therefore, deviations from a diffraction limited focus may be used to quantify non-telecentricity by taking the gradient of the aberrations measured in the Fig. 10(b) configuration.

Optics EXPRESS

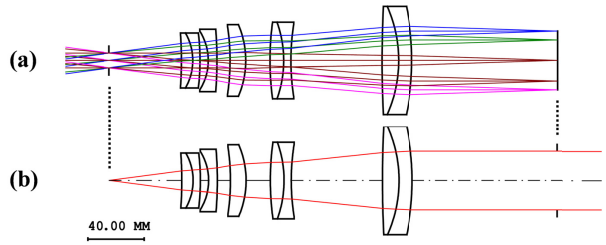

Fig. 10. Principle of the telecentricity test method demonstrated with the large FOV objective lens design shown in Fig. 5(a), reproduced here in (a). The reverse configuration is shown in (b) with the dashed lines indicating the relationship between the planes. Telecentricity may be quantified by taking the gradient of the aberrations measured in the (b) configuration.

The testing method described transforms telecentricity measurement into aberration measurement of a focusing lens system, enabling the use of existing configurations to realize the measurement in experiment. To obtain quantitative data, a Fizeau phase-shifting interferometer (PSI) may be used with the objective lens positioned in the typical fashion for system level wavefront testing (e.g. with a transmission sphere and an auto-reflecting flat optic or with a transmission flat and an auto-reflecting concave spherical optic). Alternatively, a simpler configuration for a more qualitative evaluation may be performed with a monochromatic laser and a shear plate inserted in the collimated space of Fig. 10(b). An advantage of using a shear plate is that the average slope of the wavefront is automatically obtained by principle of lateral shearing interferometry and therefore gives the average telecentricity measurement directly without further processing.

As the He-Ne wavelength of 632.8 nm was used for testing and is outside the design spectrum of the objective lens, the objective lens was re-evaluated for telecentricity as-built with the applied tolerance values. The re-tolerancing at 632.8 nm shows >90% yield is maintained at 0.02° telecentricity over the central Φ40 mm region of interest, as shown in Fig. 11(a). Once the objective lens is tested to be within specifications at the He-Ne wavelength, then almost all relevant parameters of the individual lenses and their assembly are verified except for the refractive indices. As refractive indices are slowly varying from 632.8 nm to 1080 nm (the upper bound of the NIR design wavelengths) with the maximum nominal refractive index change of 0.0251 (occurring at the last element made of S-TIH11), this remaining parameter is expected to have a negligible effect. Therefore, the telecentricity test results at the He-Ne wavelength give direct indication for the expected telecentricity performance at the NIR design wavelengths.

Due to this change in operation wavelength, it was found that there is significant back-reflection as the objective lens is AR coated for the NIR and these back-reflections caused significant data drop-out. This observation lead to the final implementation shown here where we used a commercial PSI (Verifire, Zygo Corp., PA, USA) with a F/1.5 transmission sphere (TS) and an auto-reflecting λ/10 (PV) flat silver mirror, as shown in Fig. 11(b). The use of a transmission sphere allowed the positioning of an iris diaphragm (ID15, Thorlabs Inc., NJ, USA) for spatial filtering between the PSI and the objective lens. A thin wire (not shown here) was placed between the TS and the iris to block strong unwanted back-reflections concentrated at the center of the interferogram. This wire placement was necessary as the central back-reflection was so strong that data could not be obtained otherwise. The effect of the diffraction from the wire on the final obtained interferograms is minimal as the PSI was focused to the limiting aperture of the objective lens.

The test setup was modelled in commercial optical design software to isolate the contributions to the measured aberrations resulting from the alignment of the objective lens to the PSI. The expected interferogram from telecentricity alone was found to be predominantly 3rd order spherical aberration. The objective lens was tilted and decentered as a whole to observe the resultant aberrations. It was found that the dominant alignment aberration is 3rd

Optics EXPRESS

order coma from the rotation of the lens. As such, the lens was mounted on a kinematic tip/tilt mount and the coma observed in experiment was minimized via rotational adjustments.

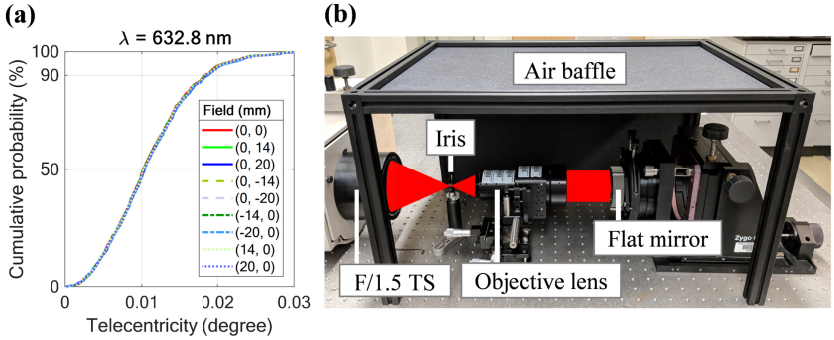

Fig. 11. (a) Re-tolerancing of the objective lens at the He-Ne testing wavelength shows larger than 90% yield at 0.02° telecentricity. (b) The experimental setup for the telecentricity testing.

To take the gradient of the measured interferogram, the lateral length dimension of the pixels must be quantified as the magnification and zoom ratios taken by the PSI internally are unknown. This step is performed after the objective lens has been well aligned to the PSI. The pixel length dimension may be quantified by imaging/measuring an object of known width in the collimated beam space between the objective lens and the auto-reflecting flat mirror. For our implementation, we inserted a digital caliper (Absolute Digimatic, Mitutoyo Corp., Japan) set to various widths into that collimated space, one instance of which is shown in Fig. 12(a) where the caliper was set to 30.00 mm. For each caliper width chosen, five measurements were taken corresponding to five independent re-positioning of the caliper at varying lateral and longitudinal locations within the space between the objective lens and the auto-reflecting flat mirror. It was found that across the range of widths tested, the variations in the extracted measurements from the images were all on the order of 1 pixel or less. In general, the larger the caliper distance, the lower the impact that this 1-pixel variation has on the length dimension, as can be seen visually from the standard deviation bars in the results shown in Fig. 12(b). The pixel length dimension was calculated to be 147.60 ± 0.40 μm/pixel, which was then used for the telecentricity calculations.

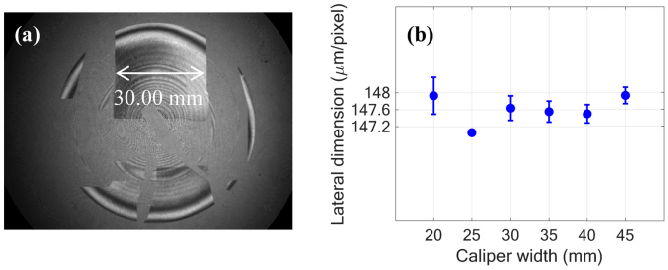

Fig. 12. (a) Image obtained with a caliper set to 30.00 mm inserted in the collimated space between the objective lens and the auto-reflecting mirror. The sharp edges of the caliper are clearly discernable and are used to extract the pixel length dimension. (b) The obtained pixel length dimension across a range of caliper widths. Using all data points, the length dimension was calculated to be 147.60 ± 0.40 μm/pixel.

A total of 50 consecutive telecentricity measurements were taken with no phase averaging for each measurement. Each measurement was processed as follows. First, the obtained phase map was cropped to the central 40 mm using the obtained pixel length dimension. Next, the data was fit to Zernike polynomials in the fringe ordering. Residual piston, tip, tilt, and power (Z1 to Z4 terms) were removed as they are purely alignment dependent. As telecentricity is in general slowly varying, orders higher than Z37 were also removed, which is analogous to

Optics EXPRESS

performing a low-pass filter on the data. The remaining Zernike terms and their corresponding fitting coefficients were then used to obtain the final telecentricity measurement after taking a gradient. The interferogram of one of the measurements is shown in Fig. 13(a) where the dominant spherical aberration is clearly visible, agreeing well with expectation. The central coma-like fringes may be due to slight tip/tilt of the lens elements within the assembly. The two-dimensional mean and standard deviation of the 50 measurements were calculated and are shown in Figs. 13(c) and 13(d) respectively. The maximum mean non-telecentricity was found to be 8.7″ with RMS of the mean of 0.8″. The maximum standard deviation is 2.2″ which is approximately four times smaller than that of the mean. The standard deviation of the pixel length dimension was found to introduce an uncertainty on the order of 0.005″, which is approximately three orders of magnitude smaller than the measured telecentricity and was therefore deemed to have a negligible effect. These results indicate that the objective lens has been fabricated and assembled well within tolerance specifications.

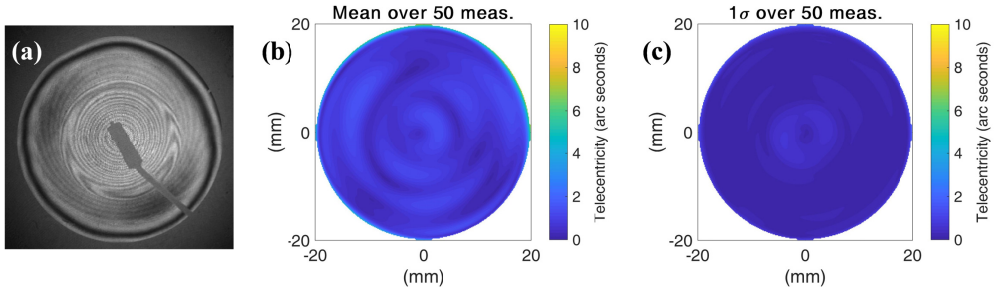

Fig. 13. (a) Interferogram of one of the telecentricity measurements, showing dominant spherical aberration as expected from simulation in optical design software. The shadow of the thin wire used to block unwanted back reflections may also be seen. (b) The mean of the 50 telecentricity measurements with maximum of 8.7″ and RMS of 0.8″. (c) The standard deviation of the 50 telecentricity measurements with maximum of 2.1″ and RMS of 0.2″.

The obtained telecentricity test results were evaluated in relation to the freeform measurement uncertainty using the simulation model presented in Section 2.1. The central Φ30 mm was used to simulate placing the Φ30 mm parabolic sample at the center of the scanning FOV. A one-dimensional slice through the two-dimensional data containing the highest non-telecentricity value within the Φ30 mm region was used. The maximum measurement error on the parabolic part was found to be 1.2 nm. If the parabola was placed toward the edge of the full FOV and experiences the largest non-telecentricity overall (i.e. 8.7″) at its steepest slope location to simulate a worst-case scenario, the maximum measurement error was found to be 11.2 nm, meeting the metrology requirement laid out in Section 1. This objective lens will be implemented in a custom OCT freeform metrology system currently in development and its measurement uncertainty contributions will be quantified in experiment with freeform optic samples.

6. Summary and discussion

In this paper, critical design requirements are detailed for the OCT sample arm in the context of low uncertainty figure metrology for freeform optical components, namely telecentricity, distortion mapping, wavefront error, and image plane flatness. Two custom objective lens systems are reported, both of which are designed with the specifications and appropriate design constraints necessary to optimize the OCT metrology system for measuring optics within a range of specifications. To maximize signal throughput, a unique pseudo-bistatic configuration was developed. This configuration also enables the integration of the two lens designs within one instrument to extend the measurement dynamic range in terms of sample slope and surface roughness.

Optics EXPRESS

One of the two lens designs reported was toleranced, fabricated, and tested for both wavefront performance and telecentricity. The single-shot telecentricity test method reported here is versatile for a range of telecentric lens configurations. For example, one may use a transmission flat and an auto-reflecting flat mirror to test a bi-telecentric lens. For a telecentric objective lens without an accessible entrance/exit pupil, for example the large NA objective lens presented here, additional steps need to be implemented to align to the internal pupil plane. Compared to the existing method of imaging a resolution target through axial distances, this method has finer angular resolution and is faster and more robust as it eliminates the large linear travel. Another interesting characteristic of this test method is that by essentially exchanging the chief ray with the marginal ray, telecentricity may be tested independently of the imaging or wavefront performance. For this method, it is crucial to know the length dimension of the pixels. A way in which the uncertainty of the telecentricity measurement may be improved is by precision machining fiducial markers of a known width apart on a component surface in the collimated space, for example the auto-reflecting flat mirror in the implementation shown here.

During the design process of the two objective lenses, it was found that there is a significant trade-off between achieving high telecentricity and diffraction limited performance over a flat image plane. To first order, telecentricity may appear straightforward to achieve by placing the entrance pupil (or the rotary mirror device in practice) at the front focal plane of the objective lens. However, it becomes apparent that aberrations will result in deviations from this first order design when one recognizes that telecentricity is, by definition, imaging the pupil plane to infinity. As with any other imaging configurations, corresponding aberrations need to be optimized for during the design process. This aspect may be further illustrated by the telecentricity test method present there. If we apply this test method to the doublet configuration shown in Fig. 3, since it is in general challenging for a single doublet to form a diffraction limited focus for a collimated beam of broad bandwidth and large diameter, it becomes intuitive that in reverse it is challenging to achieve high telecentricity with a doublet without sacrificing wavefront performance on a flat image plane over a large scanning FOV. Conversely, a lens that is designed to form a diffraction limited focus for a large diameter collimated beam may be a suitable starting point for a telecentric objective lens design. The balancing between achieving high telecentricity and diffraction limited performance on a flat image plane ultimately leads to a more complex lens design compared to a non-telecentric counterpart.

Funding

National Science Foundation (NSF) I/UCRC Center for Freeform Optics (IIP-1338877, IIP-1822049, IIP-1338898, and IIP-1822026).

Acknowledgments

We thank Julie Bentley, Changsik Yoon, and Nicholas Takaki for stimulating discussions on the design aspects of this work. Gratitude is expressed to Jonathan Papa and Michael Pomerantz for stimulating discussions on the experimental testing aspects of this work and their support in the laboratory. We thank Synopsys, Inc. for the education license of CODE V.

References

1. K. P. Thompson and J. P. Rolland, "Freeform optical surfaces: a revolution in imaging optical design," Opt. Photonics News **23**(6), 30–35 (2012).
2. J. D. Nelson, K. Medicus, and M. Brophy, "Fabricating and Testing Freeform Optics: Current Capabilities, Lessons Learned and Future Opportunities," in *Optical Fabrication and Testing* (Optical Society of America, 2014), pp. OW3B–2.
3. J. Reimers, A. Bauer, K. P. Thompson, and J. P. Rolland, "Freeform spectrometer enabling increased compactness," Light Sci. Appl. **6**(7), e17026 (2017).

Optics EXPRESS

4. S. Sorgato, R. Mohedano, J. Chaves, M. Hernández, J. Blen, D. Grabovičkić, P. Benítez, J. C. Miñano, H. Thienpont, and F. Duerr, "Compact illumination optic with three freeform surfaces for improved beam control," Opt. Express **25**(24), 29627–29641 (2017).
5. R. R. Shannon, *The Art and Science of Optical Design* (Cambridge University Press, 1997).
6. D. Xu, J. Yao, N. Zhao, and J. P. Rolland, "Scanning Customized Swept-source Optical Coherence Tomography (SS-OCT) for the Metrology of Freeform Optical Surfaces," in *Frontiers in Optics* (Optical Society of America, 2016), pp. FW5H–6.
7. J. Yao, A. Anderson, and J. P. Rolland, "Point-cloud noncontact metrology of freeform optical surfaces," Opt. Express **26**(8), 10242–10265 (2018).
8. J. Huang, Q. Yuan, B. Zhang, K. Xu, P. Tankam, E. Clarkson, M. A. Kupinski, H. B. Hindman, J. V. Aquavella, T. J. Suleski, and J. P. Rolland, "Measurement of a multi-layered tear film phantom using optical coherence tomography and statistical decision theory," Biomed. Opt. Express **5**(12), 4374–4386 (2014).
9. W. Drexler and J. G. Fujimoto, *Optical Coherence Tomography Technology and Applications* (Springer, 2008).
10. J. M. Schmitt, "Optical coherence tomography (OCT): a review," IEEE J. Sel. Top. Quant. Electron. **5**(4), 1205–1215 (1999).
11. A. F. Fercher, W. Drexler, C. K. Hitzenberger, and T. Lasser, "Optical coherence tomography-principles and applications," Rep. Prog. Phys. **66**(2), 239–303 (2003).
12. W. Drexler, M. Liu, A. Kumar, T. Kamali, A. Unterhuber, and R. A. Leitgeb, "Optical coherence tomography today: speed, contrast, and multimodality," J. Biomed. Opt. **19**(7), 071412 (2014).
13. S. Defisher, "Metrology for Manufacturing of Freeform Optical Surfaces with UltraSurf," in *Computational Optical Sensing and Imaging* (Optical Society of America, 2015), pp. JT5A–6.
14. M. A. Echter, C. D. Roll, A. D. Keene, and J. D. Ellis, "Carrier fringe analysis algorithms for three degree of freedom optical probing," Precis. Eng. **38**(4), 893–902 (2014).
15. K. Fuerschbach, G. E. Davis, K. P. Thompson, and J. P. Rolland, "Assembly of a freeform off-axis optical system employing three φ-polynomial Zernike mirrors," Opt. Lett. **39**(10), 2896–2899 (2014).
16. A. Bauer and J. P. Rolland, "Design of a freeform electronic viewfinder coupled to aberration fields of freeform optics," Opt. Express **23**(22), 28141–28153 (2015).
17. A. M. Bauer, "Optical Design with Freeform Surfaces, with Applications in Head-Worn Display Design," Ph.D. dissertation, University of Rochester (2016).